GEOPHYSICS

Unexpected far-field deformation of the 2023 Kahramanmaraş earthquakes revealed by space geodesy

S. Ergintav[1]*, P. Vernant[2], O. Tan[3], H. Karabulut[4], S. Özarpacı[5], M. Floyd[6], A. Ö. Konca[4], Z. Çakır[7], D. Acarel[8], R. Çakmak[9], H. Vasyura-Bathke[10]†, U. Doğan[5], A. İ. Kurt[11], A. Özdemir[5], E. T. Ayruk[5], M. Turğut[5], Ö. Özel[11], İ. Farımaz[5]

The spatiotemporal pattern of surface displacements from large earthquakes provides crucial insights about the deformation of Earth's crust at various scales and the interactions among tectonic plates. However, the lack of extensive and large-scale geodetic networks near such seismic events hinders our thorough understanding of the large-scale crustal deformation resulting from earthquakes. Using Türkiye's extensive and continuous global navigation satellite system (GNSS) network during the moment magnitude 7.8 and 7.6 Kahramanmaraş earthquakes on 6 February 2023, we show that large earthquakes can induce far-field crustal deformations (>700 kilometers), exceeding current predictions from elastic dislocation models. They can lead to the mobilization of tectonic plates and the triggering of far-field earthquakes, which carries profound implications for seismic hazard assessments and necessitates a new perspective on crustal deformation and earthquake mechanics.

Assessing seismic hazards is challenging, in part because it requires measuring plate motions and calculating the spatiotemporal characteristics of surface deformation along fault zones over multiple earthquake cycles (*1*–*3*). Recent advances in continuous global navigation satellite system (cGNSS) networks and synthetic aperture radar (SAR) missions have opened up many possibilities to improve understanding of fault behavior with accurate observations of surface deformation over space and time (*4*–*6*). Estimating surface deformation induced by earthquakes with elastic models serves as the backbone of the studies and provides a geophysical framework for understanding earthquake mechanics and crustal deformation (*7*–*10*). Since the 1960s, several elastic dislocation approaches have been developed and used to model earthquake-induced deformation and derive fundamental earthquake source parameters (*11*–*13*). However, despite the presence of geodetic networks and SAR coverage, documentation of crustal deformation, spanning from near to far field, caused by large continental earthquakes remains incomplete. In this context, the existence of a densely distributed cGNSS network covering Türkiye over a national and plate-scale region provides a valuable opportunity to enhance our understanding of the earthquake cycle, active tectonics in the eastern Mediterranean, and crustal deformation from near to far field resulting from the moment magnitude (M_w) 7.8 and 7.6 Kahramanmaraş earthquakes on 6 February 2023.

The Kahramanmaraş earthquake sequence offers a distinctive opportunity to understand the behavior of the left-lateral East Anatolian Fault (EAF), which forms about 600 km of the plate boundary between the Arabian and Anatolian plates (*14*, *15*). The region is characterized by its low background seismicity, relatively low geodetic strain rates, and long historical earthquake recurrence times in contrast to the other fault zones in the eastern Mediterranean region (*15*–*17*) (Fig. 1). The southern extension of the EAF connects to the Dead Sea Fault (DSF), forming a triple junction at Kahramanmaraş between the African, Anatolian, and Arabian plates (Fig. 1, top inset). At Karlıova, its northern extension joins the North Anatolian Fault (NAF) to form a second triple junction of the Arabian, Anatolian, and Eurasian plates. Historical records show that there have been severe earthquakes in eastern Türkiye as a result of the relative plate motion between Arabia and Anatolia, which ranges from 6 to 10 mm/year (*16*, *18*). The largest known earthquakes along the EAF occurred on 29 November 1114 [magnitude (M) > 7.8], 28 March 1513 (M > 7.4), and 2 March 1893 (M > 7.1). This makes the recent Kahramanmaraş sequence one of the largest earthquakes reported in the area (*14*, *15*, *17*). The activity of these large, devastating historical earthquakes contrasts with low-level activity since 1900, a period of apparent seismic quiescence. Researchers mapped creeping and locked segments, attempting to characterize the seismic quiescence that ended with the M_w 6.8 Sivrice earthquake on 24 January 2020 (*19*). The seismicity increased around the western termination of the 2020 rupture zone, and a surge of seismic activity was observed within a zone of rupture initiation before the Kahramanmaraş earthquake sequence (*20*).

The sequence began in the complex region where several tectonic structures converge to form a continental triple junction near the city of Kahramanmaraş (*21*, *22*). The first event (M_w 7.8) of this earthquake doublet initiated on the Narlı fault with a subevent of M_w 7.0 (*23*) and ruptured an ~47-km section of this fault, which is considered the northernmost segment of the DSF (*24*, *25*) or one of the northern structural members of the Hatay rift system (*26*). The Narlı rupture propagated to its intersection with the EAF after 24 s then propagated bilaterally for about 300 km. To the northeast, the rupture stopped ~20 km from the southwestern end of the M_w 6.8 Sivrice rupture. To the southwest, near Antakya Airport in the south, it ruptured segments of both the EAF and the Hatay Rift System. The second major left-lateral strike-slip event, the M_w 7.6 Elbistan earthquake, occurred 9 hours later along the Çardak and Yeşilyurt Faults west of the EAF and north of the Adana-Cilica-Hatay basin complex (Fig. 1). The M_w 7.8 and 7.6 earthquakes are hereafter referred to as the Pazarcık and Elbistan events, respectively. Their surface breaks, aftershocks, fault-plane solutions, and rupture characteristics have been extensively studied in numerous papers. Field observations, seismic and geodetic datasets, and the near-field kinematic and dynamic properties have been thoroughly discussed (*23*, *27*–*34*). These near-field studies are crucial for providing insights into the mechanisms of earthquakes and the mechanical behavior of Earth's upper layers along fault zones. While the detailed geometry and kinematics of the ruptured fault segments are of importance for the deformation in the fault vicinity, our study focuses on the far-field deformation where these details are smoothed and do not play a large role.

Nevertheless, the coseismic displacement fields of the Pazarcık and Elbistan events overlapped because of their proximity and short time interval between them relative to the period of data collection, which added complexity to the analysis of the fault zones. While this presents a challenge for interferometric SAR (InSAR) and pixel offset tracking (POT) datasets because they record both events in the same satellite

[1]Geodesy Department, Kandilli Observatory and Earthquake Research Institute (KOERI), Boğaziçi University, İstanbul, Türkiye. [2]Laboratoire Géosciences, Université de Montpellier, Montpellier Cedex 5, France. [3]Department of Geophysical Engineering, Istanbul University-Cerrahpasa, İstanbul, Türkiye. [4]Geophysics Department, Kandilli Observatory and Earthquake Research Institute (KOERI), Boğaziçi University, İstanbul, Türkiye. [5]Department of Geomatic Engineering, Yildiz Technical University, İstanbul, Türkiye. [6]Department of Earth, Atmospheric and Planetary Sciences, Massachusetts Institute of Technology, Cambridge, MA, USA. [7]Department of Geological Engineering, Istanbul Technical University, İstanbul, Türkiye. [8]Institute of Earth and Marine Sciences, Gebze Technical University, Gebze, Kocaeli, Türkiye. [9]The Earth Sciences Research Group, Vice Presidency of Climate Change and Sustainability (VPCCS), Marmara Research Center (MRC), Scientific and Technological Research Council of Türkiye (TÜBİTAK), Gebze, Kocaeli, Türkiye. [10]German Research Centre for Geosciences GFZ, Helmholtz Centre, Potsdam, Germany. [11]Geodesy Department, General Directorate of Mapping, Ankara, Türkiye.
*Corresponding author. Email: semih.ergintav@bogazici.edu.tr
†Present address: SkyGeo, Delft, Netherlands.

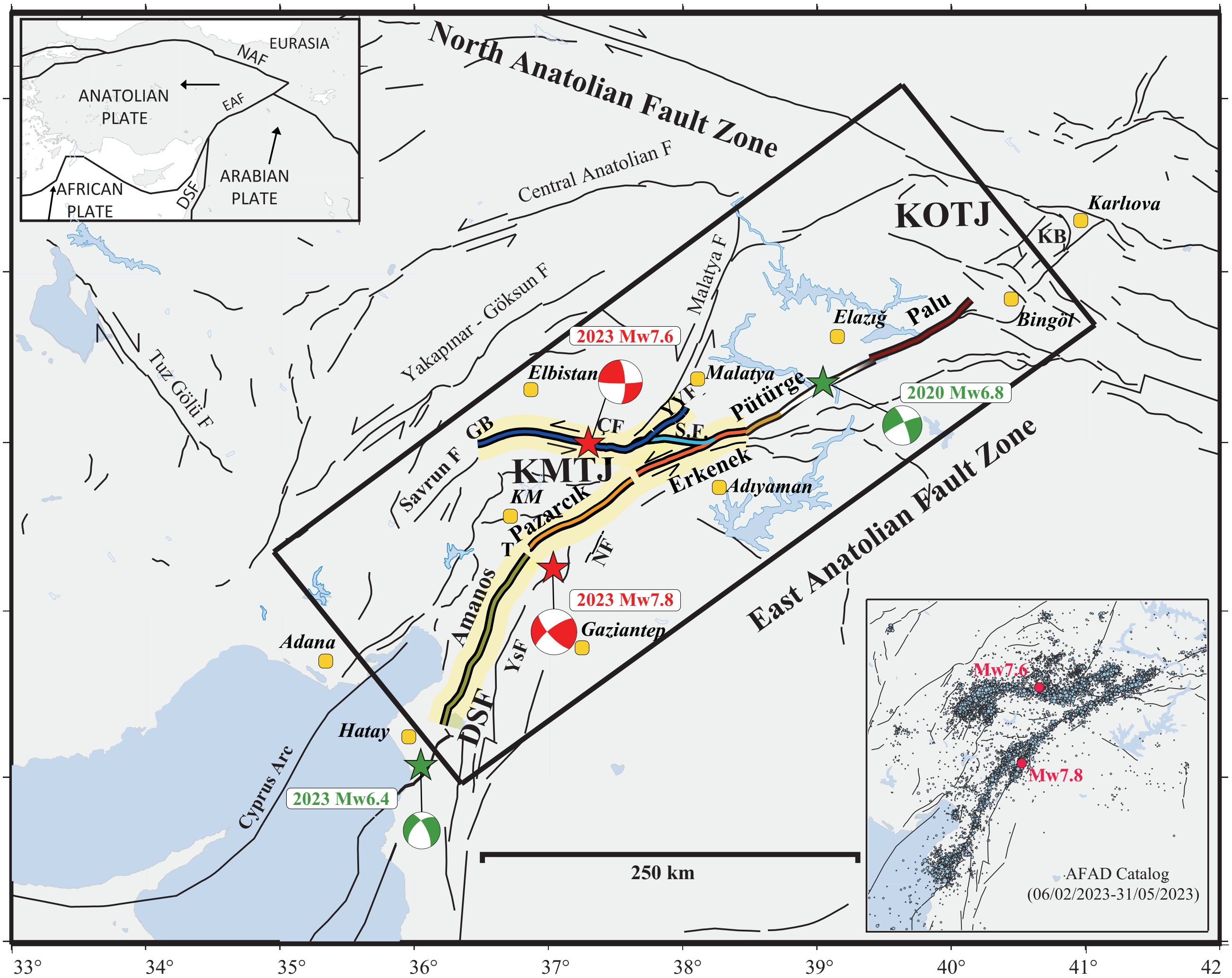

Fig. 1. Tectonic setting of the study area. Active faults are shown by black lines (*25*). Black arrows on the fault traces indicate the relative motion of the faults. Well-defined segments of the EAF are represented with different colors, and their names are shown (*14*). The green stars show the locations of the 2020 Sivrice earthquake (M_w 6.8) and the 2023 Hatay earthquake (M_w 6.4). Red stars represent the epicenters of the 2023 Kahramanmaraş earthquake sequence, and the yellow zones indicate the ruptures. The white part of the Pütürge segment illustrates the rupture zone of the 2020 Sivrice earthquake. The brown part between the Pütürge and Erkenek segments shows the unbroken part after the 2020 and 2023 events. ÇF, Çardak Fault; SF, Sürgü Fault; KMTJ, Kahramanmaraş Triple Junction; KOTJ, Karlıova Triple Junction; YsF, Yesemek Fault; NF, Narlı Fault; GB, Göksun Bend; YYF, Yeşilyurt Fault; the Karlıova Basin (KB) is also marked. The black box shows the East Anatolian Fault Zone with neighboring tectonic structures. The top-left inset shows the surrounding plates, with arrows indicating the motions relative to Eurasia. NAFZ, North Anatolian Fault Zone; EAFZ, East Anatolian Fault Zone; DSFZ, Dead Sea Fault Zone. The bottom-right inset shows the distribution of the aftershocks in the first 3 months after the Kahramanmaraş earthquakes.

acquisition, it also poses a problem for mapping geological offsets. This obstacle was effectively addressed with observations from cGNSS sites, despite the limitations of coarse spatial sampling and limited near-field coverage (*35*).

The cGNSS networks also provide the opportunity to study the spatiotemporal distributions of coseismic and postseismic fault displacements over a larger region. Their distribution of sites, from near to far field in response to major earthquakes, provides insights into the mid to lower crustal structure and the interaction from the rupture zone to the interiors of the plate by releasing strain at large distances. We estimated the far-field surface displacements from cGNSS data and determined the extent to which they remain significant with distance from the fault (fig. S1). According to elastic dislocation models (*35*), earthquakes like the M_w 7.8 Pazarcık, which had a rupture length of 400 km and extended down to 15 km, are predicted to induce relatively large surface displacements (~6 to 7 mm) within a 400-km radius of the fault (Fig. 2A). Coseismic displacements were observed to be larger than expected (~8 to 10 mm) at a considerable distance from the epicenter (~700 km), inconsistent with traditional elastic dislocation models (*7*, *28*, *33*, *36*) (Figs. 3 and 4). On the contrary, the left-lateral coseismic displacement pattern of the Elbistan event is localized around the Çardak Fault Zone (Fig. 2B), and the coseismic displacements at greater distances are lower than expected, as if the first earthquake 9 hours earlier had lowered the elastic potential within the Anatolian plate. However, the combination of modeled coseismic displacements from both earthquakes still reveals far-field deformation that exceeds expectations (Fig. 2). This discrepancy is also evident during the postearthquake period (Figs. 2C and 4).

These unexpected observations call for a reassessment of the seismic cycle, from the interseismic strain loading to the release caused by the most recent earthquakes. These discoveries

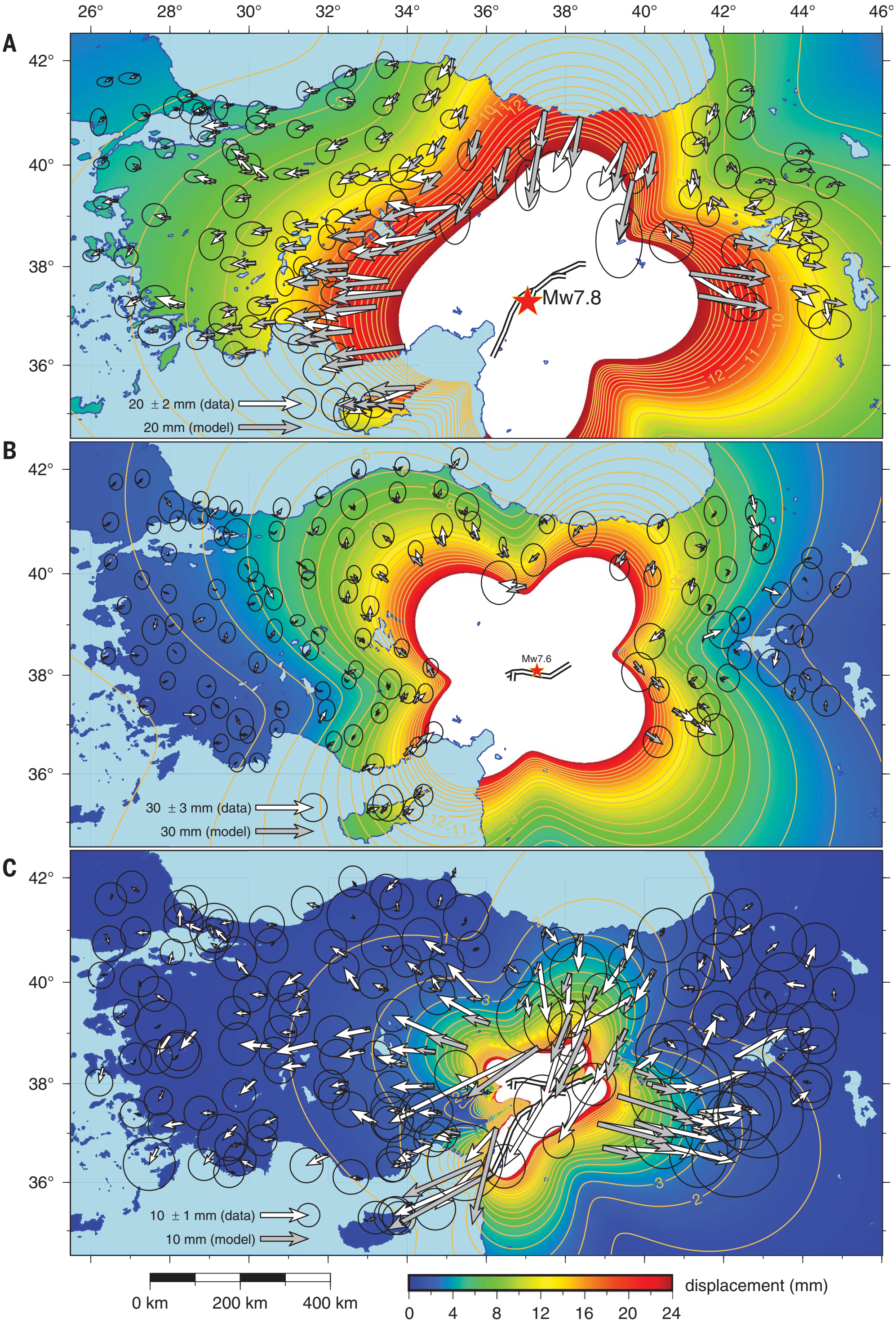

Fig. 2. Co- and postseismic displacements and 95% confidence ellipses for Pazarcık (M_w 7.8) and Elbistan (M_w 7.6) events on 6 February 2023, using layered elastic half-space models. The coseismic displacement field (white arrows) together with the simulated displacement field (gray arrows) of the estimated maximum a posteriori (MAP) slip model of the Pazarcık and Elbistan events are shown in (**A**) and (**B**), respectively. (**C**) The postseismic displacement field of the two events within the first 2 months, with the simulated displacement field obtained by the MAP of the estimated slip model. Interseismic velocities were removed using the block model in (*44*). To emphasize the far field, displacements >24 mm are not plotted. Color-coded background and contour values show the simulated displacement field, calculated from the MAP model in (*35*). Simulated displacement values do not explain observed displacements in (A) and (C) beyond ~400 km. Black double lines indicate the ruptures of Pazarcık and Elbistan events, marked with red stars and scaled with their magnitudes.

also require a reevaluation of plate-scale slip-deficit issues, mechanisms for stress transfer in large earthquakes, far field–triggered events, and earthquake cycles.

Coseismic and postseismic displacements and fault slip distributions

We present a number of datasets (*35*), with fig. S1 displaying the co- and postseismic displacement fields of the Pazarcık and Elbistan events. We removed the plate motions in the case of the postseismic displacements (showing only the displacements induced by the earthquake processes). Using this data, we built Bayesian finite-fault models and examined how the distributions of co- and postseismic slip along the rupture zones affected the static deformations in both the near and far field, using a depth-layered Earth model (*35*). We computed the Green's functions with PSGRN/PSCMP for a layered elastic half-space, which includes a correction for the effect of the curvature of Earth at larger distances (*13*). We compared the data and model for the Pazarcık and Elbistan events (figs. S7 and S8) and depict (fig. S10A) the slip distributions along the ruptures of the two events together. The models perform effectively,

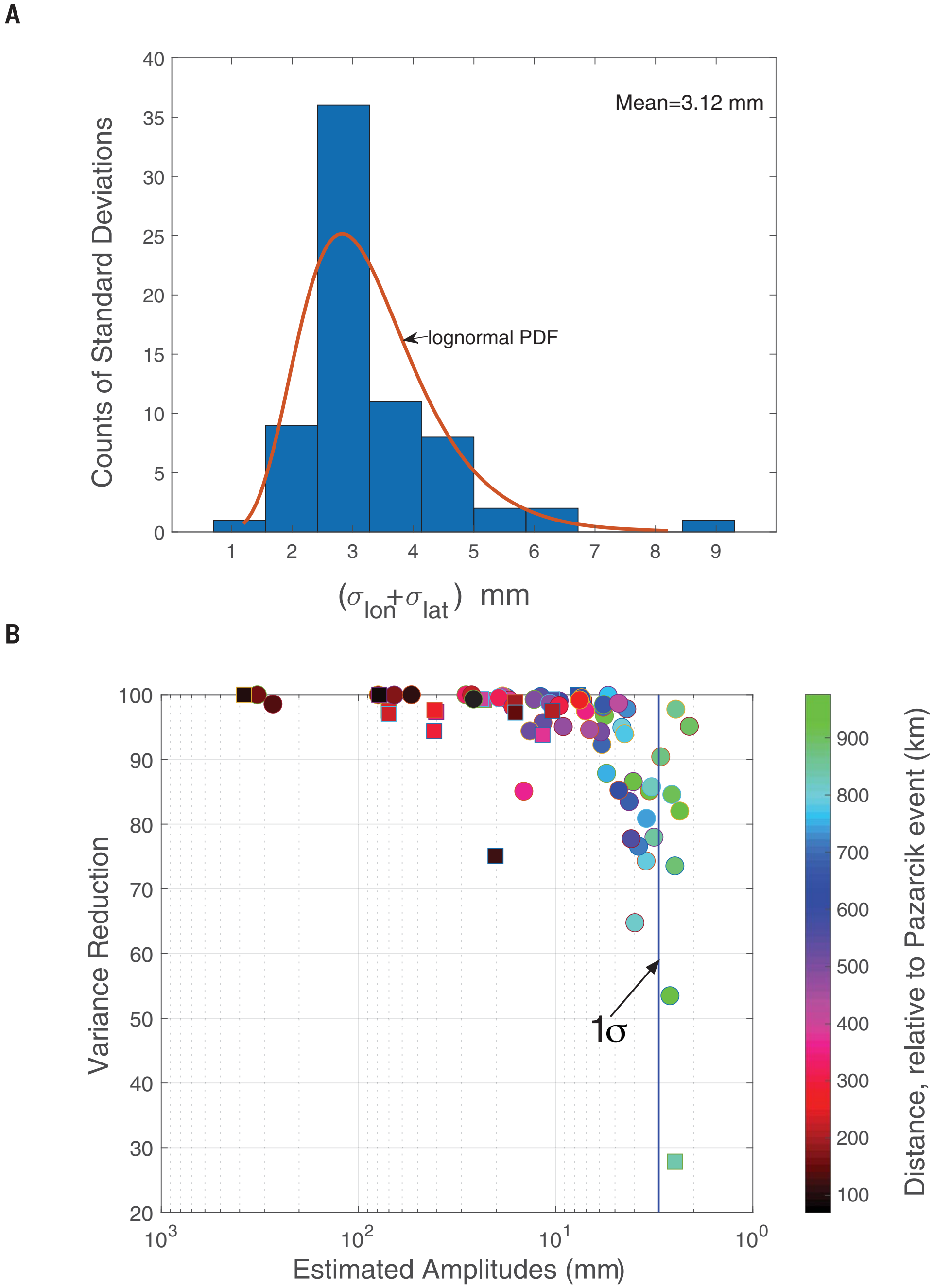

Fig. 3. Variance-reduction between the observed and estimated amplitudes from the finite-fault model with respect to the estimated amplitudes and standard deviations of observed amplitudes. (**A**) Histogram of the standard deviations of the observed amplitudes. PDF, probability density function; lon, longitude; lat, latitude. (**B**) The variance reduction (VR) (*56*) between observed amplitudes ($\overrightarrow{data}$) of coseismic displacements measured by cGNSS normalized by estimated amplitudes $\left(\overrightarrow{model}\right)$ from MAP slip model of the Pazarcık event; the original formula is simplified for a single site as $VR = \left[1 - \left(\overrightarrow{data} - \overrightarrow{model}\right)^2 / \overrightarrow{data}^2\right] * 100$. The closer the VR is to 100%, the better the data are explained by the model. Additionally, circles show the underestimated results $\left(\overrightarrow{data} - \overrightarrow{model} > 0\right)$, and squares show the overestimated ones $\left(\overrightarrow{data} - \overrightarrow{model} < 0\right)$. The VR estimates decrease when the distances from the fault to the sites increase. This is more obvious for distances >700 km, with all the VR values being underestimated. The near-field deformations are successfully estimated by the model (B), but the far-field deformations are clearly underestimated owing to the unexpected large observed amplitudes. The blue line marks the 1σ (A) limit. Beyond this line, our interpretation can be questionable, because of the noise contribution, yet we note that the observed amplitudes are still higher than the model predictions.

with variance reductions of 99.28 and 99.91%, respectively, explaining the deformations in the near field. Amplitude residuals close to the ruptures result from inelastic deformation, including localized ground failure, heterogeneities in Earth's crust, complex fault geometry, and/or incomplete near-field data. According to the depth-layered Earth model (*8*, *35*, *37*), the estimated geodetic coseismic moments for the first and second events are M_w 7.88 (M_0 = 8.1 × 10^{20} N·m) and M_w 7.66 (M_0 = 3.9 × 10^{20} N·m), respectively, which are higher than the seismic moments reported in previous studies (*30*, *31*, *38*, *39*). The moments are, however, comparable to others that use a depth-dependent shear modulus (*33*). Comparisons with the homogeneous uniform elastic half-space model are provided in (*35*).

Our coseismic static slip distributions (fig. S10A) are consistent with models that incorporate seismology, POT, and cGNSS data along the rupture (*23*, *27*, *28*, *31*–*33*), especially those located within 400 km of the rupture. Because of the limited coverage of near-field cGNSS data, we used resolution-based variable size fault discretization (*40*). A detailed discussion on the coseismic static slip distributions is provided in (*35*).

The rapid deformation transients (fig. S1C) that occurred during the first 2 months are inconsistent with the deformation rates predicted by the viscous relaxation of the broadly deforming lower crust and mainly indicate fault-parallel motions, similar to the coseismic field (*7*, *41*). Hence, we modeled the observed postseismic displacements with transient strike-slip displacement on the faults after the events, using the same procedure as we used to model the coseismic displacements (*7*, *42*). While fig. S9

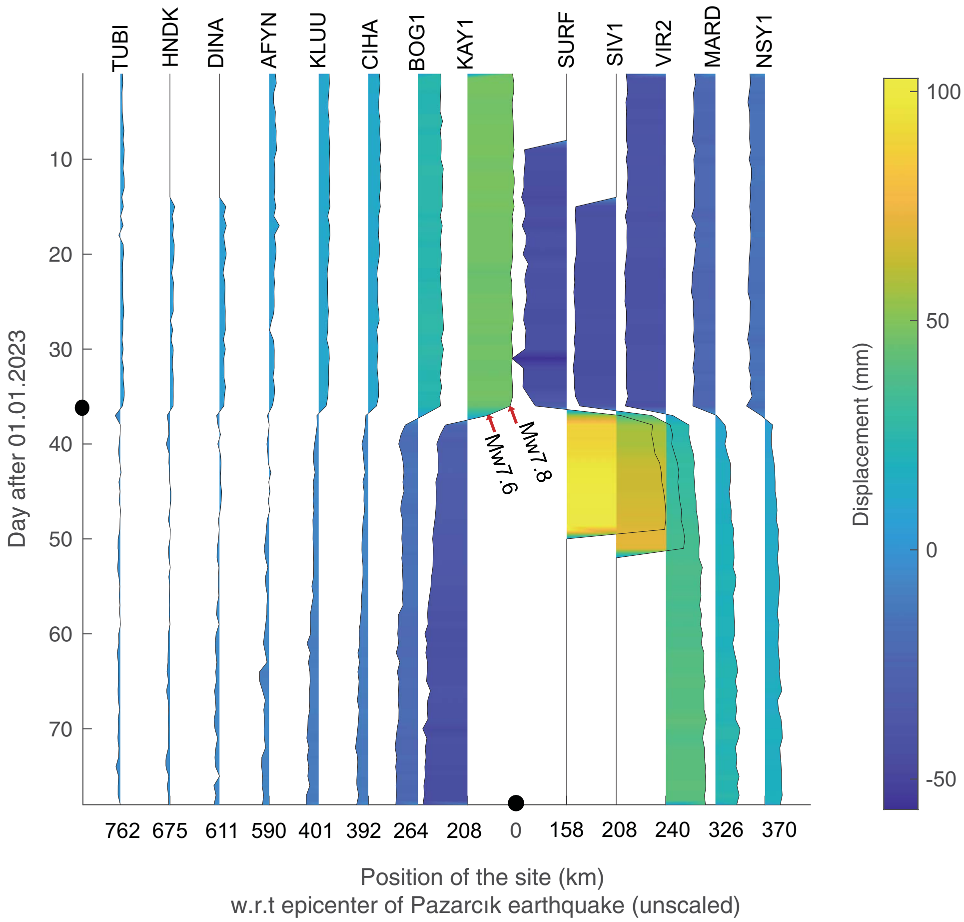

Fig. 4. East component of cGNSS time series of selected sites sorted by distance from the epicenter of M_w 7.8 to the west and the east. GNSS measurements show significant displacements in the far field (>700 km) on the order of 1 cm, which is about half a year's cumulative interseismic deformation. The site locations are nearly fault normal to the rupture zone, and their locations are indicated in fig. S1. We annotated the times of the Pazarcık (M_w 7.8) and Elbistan (M_w 7.6) events. Note that the stations SURF and SIV1 stopped collecting data after ~50 days. w.r.t., with respect to.

compares the model and data postseismic vectors, fig. S10B displays the estimated postseismic slip distributions (*35*). The kinematic postseismic model accounts for the postseismic cGNSS displacements in the near field with a 61% variance reduction. The total postseismic geodetic moment of the two events that occurred in the first 2 months is $M_0 = 1.26 \times 10^{20}$ N·m, equivalent to a M_w 7.34 earthquake. This is bigger than the cumulative seismic moment released by the aftershocks (*27*) of the two main events ($M_0 = 1.81 \times 10^{19}$ N·m and 2.97×10^{18} N·m for the Pazarcık and Elbistan events, respectively), which is equivalent to a total moment of M_w 6.82. This discrepancy indicates that considerable stress release occurred aseismically during the postseismic period.

Generally, whereas the elastic models can explain the static deformations in the near field (figs. S7 and S8), far-field deformations do not decrease with distance (Fig. 3), as expected from theory (inversely proportional to the square of distance for static displacement and inversely proportional to distance for dynamic deformations associated with body waves) (*43*). We show that the excessive far-field deformations are primarily caused by the Pazarcık event (Fig. 2, A and C) and are most noticeable during the postseismic phase. The far-field contribution of the Elbistan event is insignificant (Fig. 2B). The Pazarcık event appears to have reduced a portion of the available accumulated elastic strains, resulting in lower coseismic displacements for the Elbistan event. In the eastern portion of the Anatolian plate along the EAF, a low strain rate (<1.5 nanostrain/year) (*44*) over the past 2000 years (*45*) may indicate a full elastic "reservoir" during the preseismic stage.

Discussion and conclusions

Our analysis of the cGNSS datasets (Fig. 2 and fig. S1) indicates that the 2023 Kahramanmaraş earthquake sequence deformed the surrounding plates well beyond what can be attributed to coseismic strain release modeled with a dislocation in an elastic depth-layered Earth model. The surrounding plates exhibit different deformation patterns across their co- and postseismic fields. Our finite fault models (fig. S10) provide an explanation for the near field, but coherent far-field residuals persist (Figs. 2 and 3). For instance, both co- and postseismic observed deformations are larger than expected in the far field on the Anatolian plate at distances of >700 km (Figs. 3 and 4). In contrast, the co- and postseismic displacements on the Arabian plate are consistent with the modeled ones, reinforcing the unexpected westward motion of the whole Anatolian plate. This suggests that the Anatolian plate has moved entirely to the west relative to the Eurasian plate by ~1 cm, which is roughly equivalent to half the total offset accumulated annually. The northeastern portion of the deformed zone (i.e., the Eurasian plate) experiences lower displacements compared with the adjacent parts of the Arabian and Anatolian plates. Furthermore, the overall pattern of static deformations, supported by our models, demonstrates that the Anatolian-Arabian plate boundary is left-lateral transtensional (*44*); no present-day shortening is indicated by the deformation field (figs. S1A and S3), implying that the Anatolian plate is pulled and extending westward toward the Hellenic Subduction Zone (HSZ) rather than pushed and compressed by a currently indenting Arabian plate. This observation is inconsistent with tectonic escape models (*21*).

The coseismic, westward movement of Anatolia may also be attributed to the elastic response of thin, rigid Anatolian crust, which is underlain by a low-velocity, low-density, compliant upper mantle (*46*–*48*). We did not observe

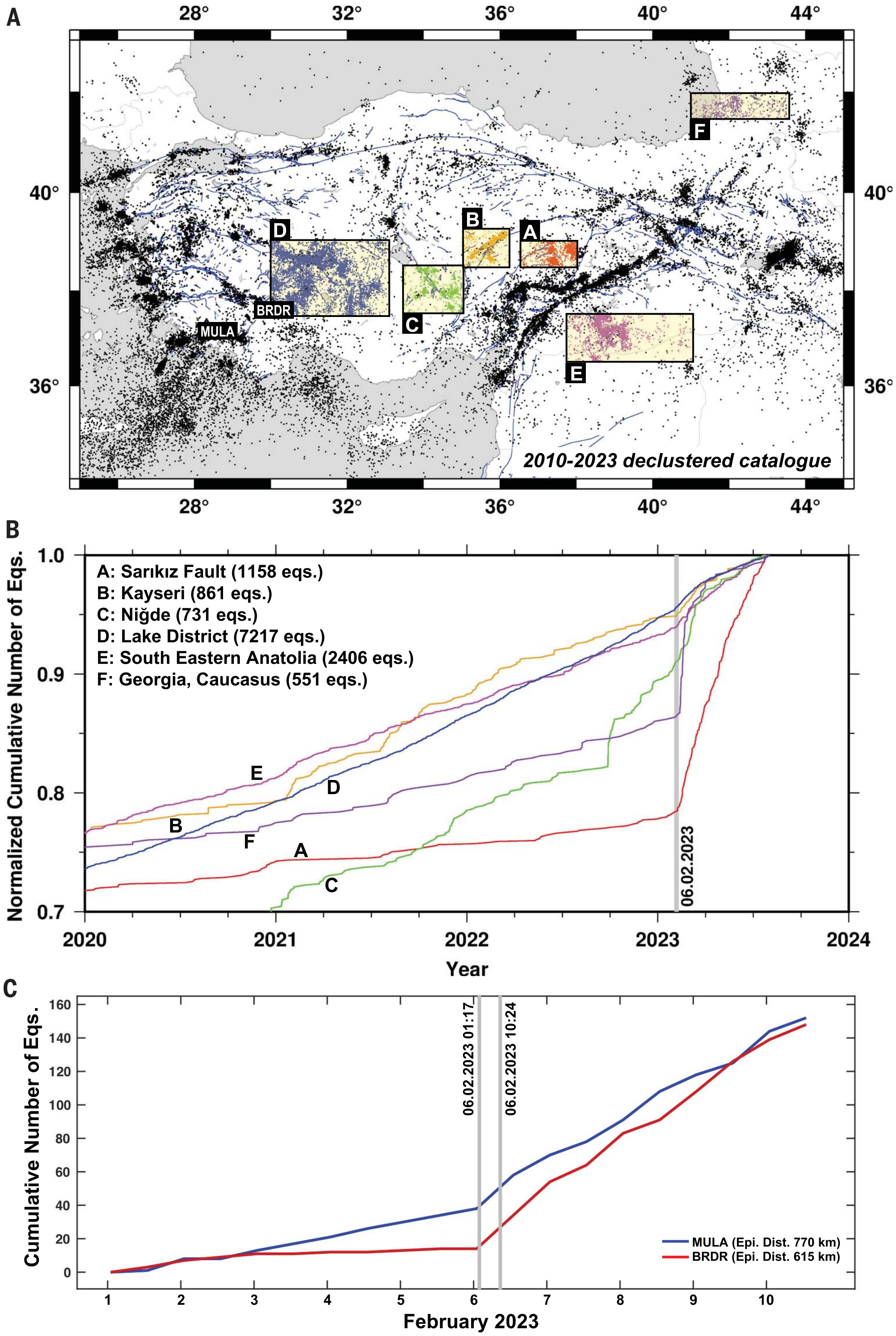

Fig. 5. The triggering of seismic activity in the far field. (**A**) Seismicity map of Türkiye since 2010 ($M \geq 3.0$) from the declustered AFAD catalog. The selected areas are labeled and colored. Blue lines are faults from the active fault map of Türkiye (*25*). (**B**) Normalized cumulative number of earthquakes ($M \geq 1.0$) in each area labeled in (A). The date of the Pazarcık event is shown with a gray bar. (**C**) The cumulative number of earthquakes detected manually at MULA and BRDR seismic stations [their locations are shown in (A)] within the first 10 days of February 2023, framing the Pazarcık event on 6 February. The *S*- to *P*-wave times are ≤6 s in order to locate the events at the stations. There is a sharp increase in seismic activity occurring in the near vicinity of these stations after the Pazarcık event. The date of the Pazarcık and Elbistan events are shown with gray bars. The continuous and catalog data are obtained from (*57*, *58*). Epi. Dist., epicentral distance.

any time-dependent propagation of deformation to the far field in the kinematic solutions of cGNSS data (fig. S4), and westward movement appears to have occurred at the onset of the first (and largest) Pazarcık event. We also did not observe dominant postseismic motions, as observed in the Arabian region. Postseismic deformations quickly disappeared (Fig. 4). These results strongly support the interpretation that the observed far-field offsets are due to the elastic response of the Anatolian plate to long-term stresses as the boundary condition has changed in the east (Figs. 2 and 3). This signature of the decoupled crust of Anatolia could result from a variety of mechanisms, including the acceleration toward the HSZ after the stress release in the east of the Anatolian plate (*49*, *50*). Therefore, the Pazarcık and Elbistan events changed the Anatolian plate's boundary conditions along the EAF and caused a westward displacement across the plate, which is under tension (*44*, *50*). This westward movement continued, faster than the secular rate, during the early postseismic period (Fig. 2C).

To the east of the rupture zone, our observations can be attributed to the collision with the Arabian foreland (figs. S1 and S3). This part of the Arabian plate is experiencing compression between the Eurasian and Arabian plates and includes several deep basins (>5 km deep), which are filled by soft sediments. Furthermore, the crustal thickness is shallower (<40 km) than in other parts of the Arabian plate (*51*). Orogenic materials (e.g., ophiolites) are further evidence of weak crust around the indentation of Arabia into the region (*51*, *52*). While the western motion of Anatolia is clear in the far field, both co- and postseismic displacements are significantly larger in the near field on the Arabian plate, displaying a clear asymmetry. A rigidity contrast and viscosity differences below the crusts of Anatolia and Arabia potentially contributed to this asymmetric pattern (*46*, *51*).

In addition, we investigated the triggering of seismic activity in the far field, which may be associated with the extensive deformation field. Due to the existence of seismic sources around and within the Anatolian and Arabian plates, as well as within the collision zone in east Anatolia between the Eurasian and Arabian plates, it was challenging to separate the background seismicity. Therefore, we looked into previously identified long-lived clusters (*53*). The locations of the selected clusters are displayed in Fig. 5A for each plate. By calculating the total number of events over the years since 2010, we illustrate the increase in activity (Fig. 5B). This shows that on the first day of the Kahramanmaraş events, all clusters were activated immediately. Afterward, we selected two sites from the far field (Fig. 5A), and we counted the number of events in the vicinity of these stations (*P-S* travel time difference < 6 s, 50 km) to observe the local response (Fig. 5C). Their temporal history shows that on the first day of the earthquake sequence, the number of earthquakes abruptly increased. This large-scale rapid seismic triggering of crustal faults appears to be another attribute of elastic plate response and supports our plate-scale cGNSS interpretations. With the relaxation of the lower crust during the postseismic period, the entire region appears to be susceptible to swarm-type seismicity and moderate-size earthquakes.

Our observations, supported by static slip models, indicate that the Kahramanmaraş earthquake sequence reveals a previously unknown class of earthquake deformation with direct implications for the mechanism of long-distance earthquake triggering and temporal variations in plate motions (*53*, *54*). This affects the earthquake hazard potential, especially for faults in and around Anatolia. To investigate the earthquake cycle of the faults along plate boundaries, an approach is needed that takes into account the deformation of entire tectonic blocks and their boundary conditions. The strain accumulated since the last earthquake can be released by a single event, yet it can also vary owing to immediate elastic responses from nearby plates. Given these factors, investigating multiple earthquake cycles becomes necessary, taking into account fault networking constraints and the coupled elastic motions of the plates, alongside the lithosphere's viscoelastic response.

From this perspective, the coupled elastic motions of the Anatolian and Arabian plates are important for understanding tectonic plate interactions and hazards within plate interiors. The stress transferred from the EAF to the NAF, for example, may tend to initiate a new earthquake cycle, as documented in the 20th century (*1*). It may also lead to an increase in seismic activity along the Zagros fold-and-thrust belt, which marks the boundary between the Eurasian and Arabian plates. One important scenario involves the interaction between the DSF and the Cyprus Arc. The occurrence of the largest aftershock (Hatay, M_w 6.4), along with co- and postseismic stress transfer (Fig. 2, A and C) to Hatay and the Cyprus Arc, marks this area as one of the highest-risk zones. Historical earthquake records indicate that major earthquakes in this region have often followed those in the Kahramanmaraş region (*55*). Furthermore, earthquakes showing surprising far-field deformation, such as the 1999 Izmit earthquake (M_w 7.6) (*4*, *7*), may require reassessment.

REFERENCES AND NOTES

1. M. N. Toksöz, A. F. Shakal, A. J. Michael, *Pure Appl. Geophys.* **117**, 1258–1270 (1979).
2. W. Thatcher, *Ann. Geophys.* **36**, 13–24 (1993).
3. T. J. Wright, J. R. Elliott, H. Wang, I. Ryder, *Tectonophysics* **609**, 504–523 (2013).
4. S. Ergintav *et al*., *J. Geophys. Res. Solid Earth* **114**, B07403 (2009).
5. J. R. Weiss *et al*., *Geophys. Res. Lett.* **47**, e2020GL087376 (2020).
6. A. O. Konca *et al*., *Bull. Seismol. Soc. Am.* **97**, S307–S322 (2007).
7. R. E. Reilinger *et al*., *Science* **289**, 1519–1524 (2000).
8. S. Heimann *et al*., *Solid Earth* **10**, 1921–1935 (2019).
9. H. Vasyura-Bathke *et al*., *Seismol. Res. Lett.* **91**, 1003–1018 (2020).
10. Y. Zhang *et al*., *Nat. Geosci.* **16**, 1054–1060 (2023).
11. K. Rybicki, *Bull. Seismol. Soc. Am.* **61**, 79–92 (1971).
12. Y. Okada, *Bull. Seismol. Soc. Am.* **82**, 1018–1040 (1992).
13. R. J. Wang, F. Lorenzo-Martín, F. Roth, *Comput. Geosci.* **32**, 527–541 (2006).
14. T. Y. Duman, O. Emre, *Spec. Publ. Geol. Soc. Lond.* **372**, 495–529 (2013).
15. S. E. Güvercin, H. Karabulut, A. O. Konca, U. Doğan, S. Ergintav, *Geophys. J. Int.* **230**, 50–69 (2022).
16. B. Aktug *et al*., *J. Geodyn.* **94–95**, 1–12 (2016).
17. S. S. Nalbant, J. McCloskey, S. Steacy, A. A. Barka, *Earth Planet. Sci. Lett.* **195**, 291–298 (2002).
18. R. Reilinger *et al*., *J. Geophys. Res. Solid Earth* **111**, B05411 (2006).
19. A. Ö Konca *et al*., *J. Geophys. Res. Solid Earth* **126**, e2021JB021830 (2021).
20. G. Kwiatek *et al*., *Nat. Commun.* **14**, 7534 (2023).
21. A. M. C. Sengör, N. Görür, *Am. Assoc. Pet. Geol. Bull* **68**, 526 (1984).
22. J. N. Meng, T. M. Kusky, E. Bozkurt, H. Deng, O. Sinoplu, *J. Earth Sci.* **35**, 758–768 (2024).
23. H. Karabulut, S. E. Guvercin, J. Hollingsworth, A. O. Konca, *J. Geol. Soc. London* **180**, jgs2023-021 (2023).
24. T. M. Kusky, E. Bozkurt, J. N. Meng, L. Wang, *J. Earth Sci.* **34**, 291–296 (2023).
25. Ö. Emre *et al*., Active fault map of Turkey with an explanatory text, General Directorate of Mineral Research and Exploration, Special Publication Series-30 (2013); https://www.mta.gov.tr/en/maps/active-fault-1250000.
26. A. M. C. Şengör, C. Zabcı, B. A. Natal'in, in *Transform Plate Boundaries and Fracture Zones*, J. C. Duarte, Ed. (Elsevier, 2019), pp. 169–247.
27. S. Ezgi Güvercin, *Seismol. Res. Lett.* **95**, 664–679 (2024).
28. S. Barbot *et al*., *Seismica* **2**, 1–17 (2023).
29. V. Karabacak *et al*., *J. Geol. Soc. London* **180**, jgs2023-020 (2023).
30. D. Melgar *et al*., *Seismica* **2**, 1–10 (2023).
31. L. Dal Zilio, J.-P. Ampuero, *Commun. Earth Environ.* **4**, 71 (2023).
32. P. M. Mai *et al*., *The Seismic Record* **3**, 105–115 (2023).
33. Z. Jia *et al*., *Science* **381**, 985–990 (2023).
34. J. Meng *et al*., *Science* **383**, 298–305 (2024).
35. Materials and methods are available as supplementary materials.
36. J. J. Zhao, Q. Chen, Y. H. Yang, Q. Xu, *Remote Sens.* **15**, 3327 (2023).
37. W. B. Xu, R. Burgmann, Z. W. Li, *Geophys. J. Int.* **205**, 236–242 (2016).
38. C. Ren *et al*., *Science* **383**, 305–311 (2024).
39. R. Okuwaki, Y. Yagi, T. Taymaz, S. P. Hicks, *Geophys. Res. Lett.* **50**, e2023GL103480 (2023).
40. S. Atzori, A. Antonioli, *Geophys. J. Int.* **185**, 529–538 (2011).
41. E. H. Hearn, S. McClusky, S. Ergintav, R. E. Reilinger, *J. Geophys. Res. Solid Earth* **114**, B08405 (2009).
42. Z. Çakır *et al*., *Geophys. J. Int.* **155**, 93–110 (2003).
43. K. Aki, P. G. Richards, *Quantitative Seismology* (University Science Books, 2002).
44. S. Ergintav *et al*., *Turk. J. Earth Sci.* **32**, 248–261 (2023).
45. T. Sançar, C. Zabci, V. Karabacak, M. Yazici, H. S. Akyüz, *J. Seismol.* **23**, 319–340 (2019).
46. A. K. Mutlu, H. Karabulut, *Geophys. J. Int.* **187**, 1743–1758 (2011).
47. I. M. Artemieva, A. Shulgin, *Tectonics* **38**, 4465–4487 (2019).
48. H. Karabulut, A. Paul, A. D. Ozbakir, T. Ergun, S. Senturk, *Geophys. J. Int.* **218**, 57–73 (2019).
49. R. Reilinger, S. McClusky, *Geophys. J. Int.* **186**, 971–979 (2011).
50. L. Jolivet *et al*., *Tectonophysics* **597–598**, 1–33 (2013).
51. A. Kaviani *et al*., *Geophys. J. Int.* **221**, 1349–1365 (2020).
52. E. Türkoğlu, M. Unsworth, I. Çağlar, V. Tuncer, Ü. Avşar, *Geology* **36**, 619–622 (2008).
53. H. Karabulut, M. Bouchon, J. Schmittbuhl, *Earth Planets Space* **74**, 158 (2022).
54. J. Gomberg, P. Bodin, K. Larson, H. Dragert, *Nature* **427**, 621–624 (2004).
55. N. N. Ambraseys, *Earthquakes in the Mediterranean and Middle East: A Multidisciplinary Study of Seismicity up to 1900* (Cambridge Univ. Press, 2009).
56. H. Vasyura-Bathke *et al*., *Seismica* **3**, 1–18 (2024).
57. Disaster and Emergency Management Authority, Turkish National Seismic Network [Dataset], Department of Earthquake, Disaster and Emergency Management Authority (1990); https://doi.org/10.7914/SN/TU.
58. Kandilli Observatory And Earthquake Research Institute, Boğaziçi University, Kandilli Observatory and Earthquake Research Institute (KOERI) [Dataset], International Federation of Digital Seismograph Networks (1971); https://doi.org/10.7914/SN/KO.

ACKNOWLEDGMENTS

We are grateful to R. Reilinger for invaluable feedback, which considerably enhanced the initial manuscript. We thank T. Kusky and an anonymous reviewer for providing valuable comments and suggestions that improved the manuscript. We thank the General Directorate of Mapping and the General Directorate of Land Registry and Cadastre for providing daily and high-rate GNSS data from the CORS-TR (TUSAGA-Aktif) network used in this study (https://www.tusaga-aktif.gov.tr/Web/DepremVerileri.aspx) and the Disaster and Emergency Management Authority (AFAD) for making available the seismic waveform data and the earthquake catalogs used in this study (*57*). Waveform and catalog data from the seismic stations operated by Bogazici University, Kandilli Observatory and Earthquake Research Institute, Regional Earthquake-Tsunami Monitoring Center (*58*) were also used. The numerical calculations reported in this paper were fully performed at the TUBITAK ULAKBIM, High Performance and Grid Computing Center (TRUBA resources). **Funding:** The Scientific and Technological Research Council of Türkiye (TÜBİTAK) ARDEB 1001 Research Projects Programme no. 121Y400; TÜBİTAK 1002C Natural Disasters Focused Fieldwork Emergency Support Program no. 123D003; TÜBİTAK MRC Post-earthquake Emergency Observation Research (DEPAR-II) no. 5207901. **Author contributions:** Conceptualization: S.E. (lead), P.V., O.T., H.K., and A.Ö.K. Methodology: S.E., P.V., O.T., H.K., A.Ö.K., S.Ö., U.D., A.İ.K., and H.V.-B. Investigation: S.E. (lead), P.V., O.T., H.K., A.Ö.K., and Z.Ç. Formal analysis: S.E., P.V., D.A., R.Ç., O.T., M.F., Ö.Ö., A.Ö., E.T.A., İ.F., M.T., and A.İ.K . Visualization: S.E., O.T., D.A., P.V., M.F., A.Ö.K., S.Ö., and H.V.-B. Resources: S.E., U.D., A.İ.K., and R.Ç. Data curation: A.İ.K., Ö.Ö., A.Ö., and M.T. Writing – original draft: S.E. (lead), P.V., H.K., M.F., Z.Ç., O.T., and A.Ö.K. Writing – review & editing: S.E. (lead), P.V., H.K., M.F., Z.Ç., U.D., D.A., O.T., and H.V. **Competing interests:** The authors declare that they have no competing interests. **Data and materials availability:** The regional seismic data are publicly available (*57*, *58*). The GNSS data are also publicly avaliable from the CORS-TR (TUSAGA-Aktif) network used in this study (https://www.tusaga-aktif.gov.tr/Web/DepremVerileri.aspx). Geodetic data required to reproduce the results are available in the supplementary materials.

SUPPLEMENTARY MATERIALS

science.org/doi/10.1126/science.ado4220
Materials and Methods
Figs. S1 to S10
Tables S1 to S3
References (*59*–*63*)

Submitted 16 March 2024; accepted 12 September 2024
10.1126/science.ado4220